Petrography and the REE-composition of apatite in the Paleoproterozoic Pilgujärvi Sedimentary Formation, Pechenga Greenstone Belt, Russia

Lauri Joosu[a,], Aivo Lepland[a, b, c, d], Timmu Kreitsmann[a], Kärt Üpraus[d], Nick M.W. Roberts[e], Päärn Paiste[a], Adam P. Martin[e, 1], Kalle Kirsimäe[a]

[a] University of Tartu, Department of Geology, 50411 Tartu, Estonia

[b] Geological Survey of Norway, 7491 Trondheim, Norway

[c] Tallinn University of Technology, Institute of Geology, 19086 Tallinn, Estonia

[d] Centre for Arctic Gas Hydrate, Environment and Climate, University of Tromsø, 9037 Tromsø, Norway

[e] NERC Isotope Geosciences Laboratory, British Geological Survey, Keyworth, Nottingham NG12 5GG, UK

Geochimica et Cosmochimica Acta

Volume 186, 1 August 2016, Pages 135–153

Abstract

The first globally significant phosphorous-rich deposits appear in the Paleoproterozoic at around 2 Ga, however, the specific triggers leading to apatite precipitation are debated. We examine phosphorous-rich rocks (up to 8 wt% P_2O_5) in 1.98–1.92 Ga old Pilgujärvi Sedimentary Formation, Pechenga Greenstone Belt, Russia. Phosphates in these rocks occur as locally derived and resedimented sand-to-gravel/pebble sized grains consisting of apatite-cemented muddy sediments. Phosphatic grains can be subdivided into four petrographic types (A–D), each has a distinct REE signature reflecting different early-to-late diagenetic conditions and/or metamorphic overprint. Pyrite containing petrographic type D, which typically has a flat REE pattern, negative Ce anomaly and positive Eu anomaly, is the best preserved of the four types and best records conditions present during apatite precipitation. Type D phosphatic grains precipitated under (sub)oxic basinal conditions with a significant hydrothermal influence. These characteristics are similar to Zaonega Formation phosphates of NW Russia's Onega Basin, and consistent with phosphogenesis triggered by the development of anoxic(sulfidic)–(sub)oxic redoxclines at shallow sediment depth during the Paleoproterozoic.

Keywords

Sedimentary apatite;

Laser ablation inductively coupled plasma mass spectrometry;

Rare Earth Element;

Cerium anomaly;

Europium anomaly;

Paleoproterozoic

1. Introduction

Phosphorus is an essential and non-substitutable element for life: it is a key component in deoxyribo- and ribonucleic acids that hold and transfer genetic "memory" and in adenosine triphosphate (and its precursor molecules) that drive energy systems. Phosphorous is one of the most important primary productivity limiting nutrients (Tyrell, 1999, Planavsky et al., 2010, Vitousek et al., 2010 and Pufahl and Hiatt, 2012) and there is global demand for phosphorous as a natural resource (Peñuelas et al., 2013).

In the natural P-cycle continental weathering delivers most phosphorous to oceans via fluvial transport (Filippelli, 2002 and Filippelli, 2008). The concentrations of dissolved phosphorus in most surface seawaters are near zero (Filippelli, 2008) because photic zone primary producers efficiently use the reactive (dissolved) phosphorous (Fröelich et al., 1982 and Ammerman et al., 2003). Phosphorous is removed from seawater via organic matter sedimentation, as well as by scavenging onto iron–manganese oxide particles (Filippelli, 2008). Within sediments P is released into pore water during diagenetic mineralization of organic matter and reductive dissolution of iron–manganese oxides enabling authigenic P minerals to form (Ruttenberg, 2003). Major phosphorous sinks and P-rich deposits – phosphorites – occur at continental margins and/or in coastal areas influenced by ocean upwelling currents. At these locations P-rich deep ocean water stimulates primary production leading to deposition of organic-rich sediments with organically bound polyphosphate; modern examples of this are the Namibian and the Peruvian shelves (Föllmi, 1996).

Phosphorites are common in the Phanerozoic, but the first significant P-rich deposits appear in the Paleoproterozoic, with several deposits occurring at around 2 Ga (Bekker and Eriksson, 2003 and Papineau, 2010). The Paleoproterozoic P-rich deposits have been linked to oxidation of the atmosphere and establishment of the modern-like aerobic Earth at about 2.3 Ga, the Great Oxidation Event (GOE, Bekker et al., 2004, Canfield, 2005 and Bekker and Holland, 2012). The GOE led to extensive continental weathering and an associated increase of reactive phosphorous discharged to the ocean triggering a bloom of primary producers (Holland, 2002, Melezhik et al., 2005, Papineau, 2010,Bekker and Holland, 2012, Pufahl and Hiatt, 2012 and Martin et al., 2015). However, there is a gap of 200–300 Ma between GOE and the appearance of the first phosphorites. This time gap has been explained by the slow build-up of seawater sulfate concentration and development of sharp redoxclines within the upper few centimeters of sediment, needed for diagenetic P cycling and phosphogenesis (Lepland et al., 2014). During formation of oldest phosphorites a speculative drop in atmospheric oxygen has been inferred (Bekker and Holland, 2012 and Partin et al., 2013), of which the causes, however, are poorly understood (e.g. Lyons et al., 2014). Hence the

possible links between atmospheric oxygen fluctuations to the formation of the first phosphorites remain conjectural.

Apart from a specific mechanism e.g. Fe/Mn redox cycling and mineralization of organic matter by bacterial sulfate reduction and/or emergence of habitats for sulfur-bacteria (Krajewski et al., 1994, Schulz and Schulz, 2005, Nelson et al., 2010 and Lepland et al., 2014), the phosphate concentration and precipitation during the Paleoproterozoic would have required establishment of suboxic or oxic seawater conditions and, most importantly, development of fluctuating redox conditions in sediments that is crucial for concentrating interstitial phosphate.

Recently, Lepland et al. (2014) suggested that sulfur–oxidizing bacteria living at (sub)oxic–anoxic redoxcline at shallow sediment depth in consortium with methanotrophic archaea were present and possibly concentrating the interstitial phosphate in the Zaonega Formation, Onega Basin, Karelia, NW-Russia (Fig. 1). The age of the Zaonega Formation is broadly constrained between 2.06 and 1.96 Ga, with some workers suggesting deposition occurred at ca. 1.97 Ga (Puchtel et al., 1999 and Martin et al., 2015). Organic-rich mudstone and dolostone intervals of the Zaonega Formation host one of the earliest phosphorite occurrences [P_2O_5 content locally up to 15 weight percent (wt%), Lepland et al., 2014].

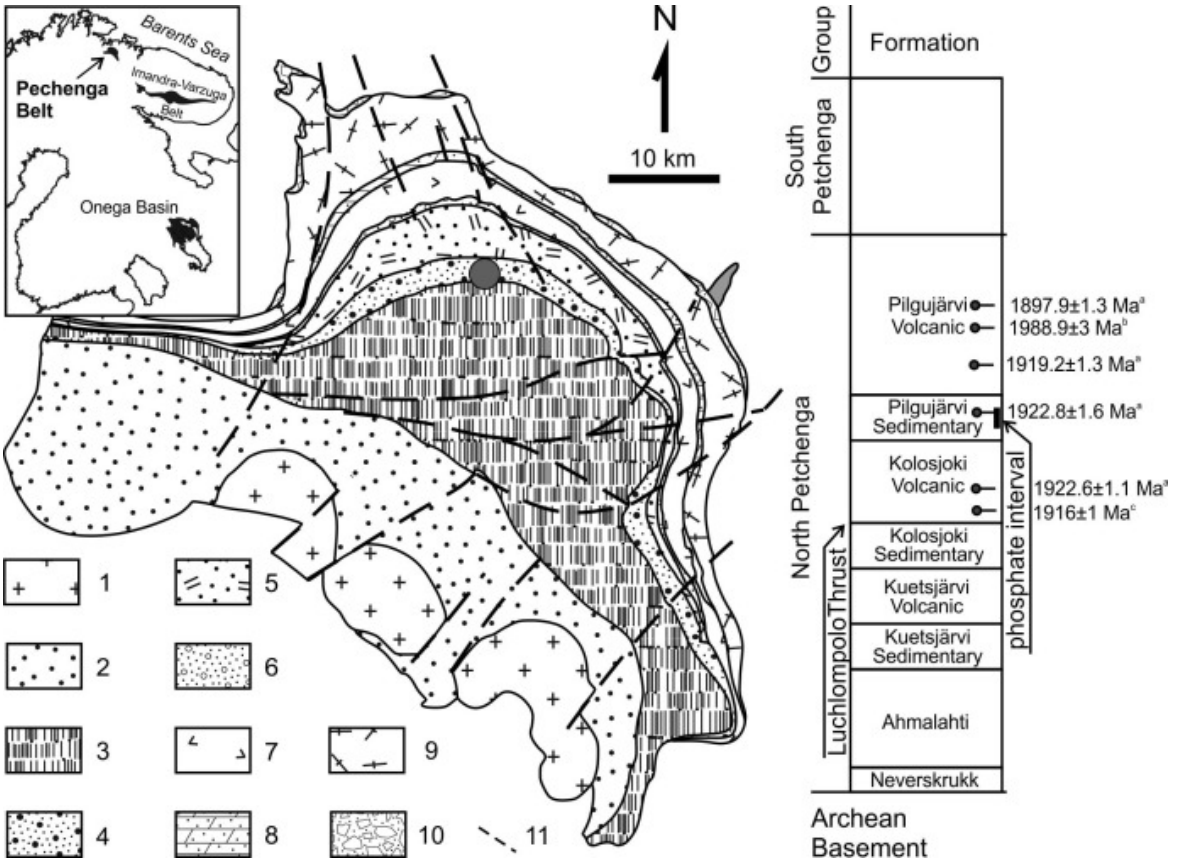

Fig. 1. Simplified geological map of the Pechenga Greenstone Belt (modified from Hanski et al., 2014). Legend: 1 – granodiorite intrusives, 2 – South Petchenga Group, 3 – Pilgujärvi Volcanic Formation, 4 – Pilgujärvi Sedimentary Formation, 5 – Kolosjoki Volcanic Formation, 6 – Kolosjoki Sedimentary Formation, 7 – Kuetsjärvi Volcanic Formation, 8 – Kuetsjärvi Sedimentary Formation, 9 – Ahmalahti Formation, 10 – Neverskukk Formation, 11 – faults. Dates are from (a) Martin et al. (2015), (b) Hanski et al. (2014), (c)Gärtner et al. (2011).

Another occurrence of Paleoproteorzoic P-bearing rocks is the phosphorous-rich (up to 8 wt% P_2O_5) gritstone-sandstone layers in the Paleoproterozoic Pilgujärvi Sedimentary Formation (SF) in the Pechenga Greenstone Belt of the Kola Peninsula, Russia (Akhmedov, 1973 and Lepland et al., 2013). The age of the Pilgujärvi SF is broadly constrained between 1.98 and 1.92 Ga (Hanski et al., 1990, Hanski et al., 2014, Hannah et al., 2006 and Martin et al., 2015). Whereas Zaonega phosphates occur mainly *in situ*, forming layers and lenses in bedded mudstones, the Pilgujärvi SF phosphates occur as detrial, phosphatic, sand-to-gravel/pebble size grains transported and redeposited either in environments interpreted to range from deltaic (Bekasova, 1985) to continental slope turbidite fan settings (Akhmedov and Krupenik, 1990 and Melezhik and Sturt, 1998).

The origin and environmental context of the phosphate precipitation in the Pilgujärvi SF is poorly understood. However, Rozanov et al. (2007) and Rozanov and Astafieva (2008)have described abundant and diverse remains of putative fossilized filamentous, coccoid, oval and rod-shaped microorganisms in the phosphatic grains from the Pilgujärvi SF. Morphology of the described microbial structures resemble cyanobacteria reported from modern alkaline or saline environments, suggesting possibly that cyanobacterial mat structures were the sites for phosphogenesis in the Pilgujärvi SF (Rozanov and Astafieva, 2008).

Here we report the microfabric of the Pilgujärvi SF phosphatic grains and the Rare Earth Element (REE) abundances in apatite to assess the environmental conditions of phosphogenesis. The REEs are incorporated into the sedimentary apatite structure during early diagenetic precipitation and reflect compositions of sediment pore water and the overlaying water column (Jarvis et al., 1994). Furthermore, the relative enrichment and/or depletion of redox-sensitive REE element Ce can be used for interpreting the redox state of phosphogenetic environments. The aim of this study is to compare and contrast the environmental redox conditions recorded in the Pilgujärvi SF apatite with the suboxic-to-anoxic redox conditions inferred for the depositional setting of the Zaonega Formation (Joosu et al., 2015).

2. Geological setting

The Pechenga Greenstone Belt (Fig. 1) belongs to the ca. 800 km long chain of Transfennoscandian Paleoproterozoic greenstone belts extending from the eastern Kola Peninsula, Russia, to northern Norway (Melezhik and Sturt, 1994 and Melezhik and Hanski, 2013). The geology of the area has been recently and comprehensively reviewed in Melezhik and Hanski (2013). The North Pechenga Group, developed in the northern part of the greenstone belt, is composed of eight lithostratigraphic units (Fig. 1) including the Pilgujärvi SF and Pilgujärvi Volcanic Formations. The Pechenga Greenstone Belt underwent regional, greenschist facies metamorphism during the Svecofennian Orogeny at 1.89–1.79 Ga (Melezhik and Hanski, 2013).

The Pilgujärvi SF is the thickest sedimentary succession (up to 1000 m) of the Pechenga Greenstone Belt (Fig. 1) and is dominated by rhythmically interbedded C_{org}- and sulfide-rich turbiditic greywacke, shales and tuffs deposited in a deep-water, shelf environment (Akhmedov and Krupenik, 1990 and Melezhik and Sturt, 1998). It hosts numerous mafic-ultramafic sills and minor lavas, reaching a total thickness of ca. 500 m and houses the large

reserves of Pechenga Ni–Cu-sulfide deposits along the contact zones of sills and sedimentary host rocks (Melezhik and Hanski, 2013).

Phosphorus-rich intervals occur as lenses and a series of gritstone and coarse-grained sandstone beds within a 50–250 m-thick rhythmically bedded facies in the central part of the Pilgujärvi SF (Bekasova and Dudkin, 1981). Rounded to angular phosphatic grains (0.1–6 mm in size) typically occur in the coarser-grained, lower parts of beds together with grains of quartz [40–54 volume (vol%)], feldspar (7–10 vol%), quartzite-silicified shale (7–30 vol%) and lithic clasts of mafic lava (3–30 vol%) (Bekasova and Dudkin, 1981, Fig. 2). The phosphatic grains form less than 5 vol% of the gritstone (Lepland et al., 2013) and are composed of carbonate-fluor apatite (francolite) that cements fine-grained sediments containing a varying admixture of quartz, feldspar, mica, pyrite, mudstone fragments and organic matter (3–5 wt%, Bekasova and Dudkin, 1981). Locally, the P-rich gritstones show high abundances of clasts rich in pyrite and pyrrhotite (>50 vol% in places), with sizes from <1 mm to 20 mm, including outsized, angular or rounded and softly-deformed fragments of bedded and laminated siltstone and mudstone (Lepland et al., 2013).

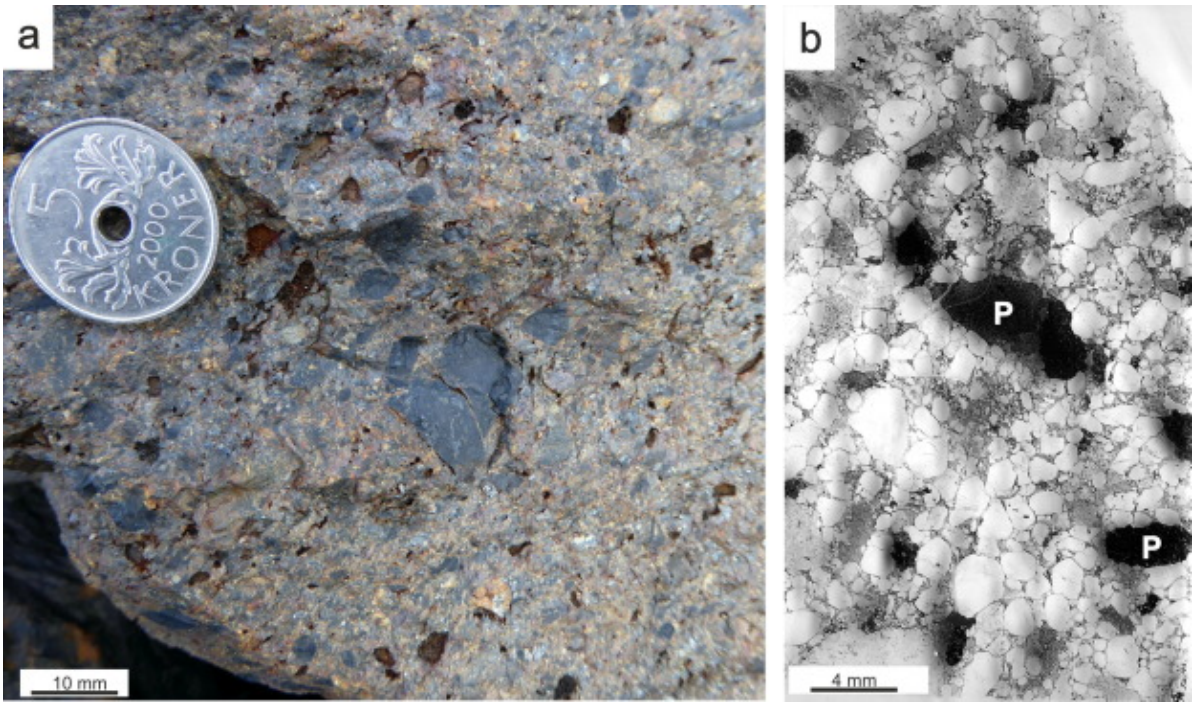

Fig. 2. Photograph of handspecimen (a) and optical image of thin section (b) of gritstone. The gritstone comprises siltstone, quartz, feldspar, and phosphatic grains (black grains in (a) and grains marked with P in (b)).

The relatively large size of the phosphatic grains, along with other abundant, locally derived clasts (e.g. mudstone and pyrite), indicate a short transport distance (Lepland et al., 2013).

The Kolosjoki Volcanic Formation, stratigraphically beneath the Pilgujärvi SF, is dated at 1922.6 ± 1.1 Ma by the isotope dilution thermal ionization mass spectrometry (ID-TIMS) method on zircon (Martin et al., 2015) and the underlying upper Kolosjoki Sedimentary Formation yields detrital zircon grains dated at 1916 ± 1 Ma (ID-TIMS, Gärtner et al., 2011). Detrital zircon grains sampled from near the base of the Pilgujärvi SF, provide a maximum age to deposition of 1922.8 ± 1.6 Ma (ID-TIMS, Martin et al., 2015) and various single isochron methods on mafic intrusions and organic-rich shales provide a range of ages

between 2231 and 1924 Ma (Hanski et al., 1990, Walker et al., 1997 and Hannah et al., 2006), with the older ages inferred to be due to inheritance (Martin et al., 2015). Zircon grains in a tuff in the Pilgujärvi Volcanic Formation, immediately overlying the Pilgujärvi SF, have yielded a 1919.2 ± 1.3 Ma age (Martin et al., 2015). A felsic lava flow higher in the Pilgujärvi Volcanic Formation has been dated at 1897.9 ± 1.3 Ma (Martin et al., 2015). Likely xenocrystic zircon grains have previously yield a maximum 1988 ± 3 Ma date from a felsic tuff in the same section by the secondary ion mass spectrometry (SIMS) method (Hanski et al., 2014). In summary, the age of the Pilgujärvi SF is constrained to between 1.98 and 1.92 Ga, with recent work suggesting deposition around 1.92 Ga.

3. Material and methods

Pilgujärvi SF P-rich rocks have not been observed in natural outcrops but have been documented in drill cores (Bekasova and Dudkin, 1981, Melezhik and Sturt, 1998 and Lepland et al., 2013) and have been locally displaced into spoil tips during open-pit mining of Cu–Ni sulfide ores. One such spoil tip (69° 24′35″N, 30° 38′15″E) ca. 7 km WSW of Zapolyarny comprises numerous meter scale, fresh blocks of rhythmically bedded greywacke- sandstone–siltstone with gritstone–sandstone intervals containing abundant phosphatic grains. Lithological similarities between P-rich gritstone–sandstone horizons in drill cores and within these blocks suggests that they were likely derived from the middle part of the Pilgujärvi SF, although the exact stratigraphic position remains unknown. Samples used in this study were collected from five different blocks.

The mineralogical composition of whole rock samples was studied by means of X-ray diffractometry (XRD). Samples were pulverized in a planetary mill and unoriented preparations were made. Preparations were scanned on a Bruker D8 Advance diffractometer using Cu*K*α radiation and LynxEye positive sensitive detector in 2–70° 2Theta range. The quantitative mineralogical composition of the samples was interpreted and modeled by using the Rietveld algorithm-based program Siroquant-3 (Taylor, 1991). The P_2O_5 concentrations in whole-rock samples were analysed using a X-ray fluorescence (XRF) Rigaku Primus II spectrometer in pressed powdered samples.

Polished slabs and petrographic thin sections were prepared and studied with a petrographic optical microscope and a scanning electron microscope (SEM) at the University of Tartu, Estonia, using a variable pressure Zeiss EVO MA15 SEM equipped with Oxford X-MAX energy dispersive detector system and AZTEC software for element analysis.

The REE in apatite were measured at the Natural Environment Research Council Isotope Geosciences Laboratory, Nottingham (NIGL) and Department of Geology, University of Tartu, by laser ablation inductively coupled plasma mass spectrometry (LA-ICP-MS). In total, 56 spots were analysed from polished slabs. Measurements at NIGL were performed using a Nu Instruments AttoM single-collector ICP-MS in linkscan mode, coupled to a New Wave Research UP193ss with a fast-washout two-volume large-format cell. Typical ablation parameters at NIGL included a 35 µm spot, at 5 Hz and ~2.5 j/cm^{2}fluence, with a 40 s dwell time. Measurements at the University of Tartu were made using an Agilent 8800 quadrupole ICP-MS coupled to a Cetac 213 nm HelEx fast-washout two-volume large-format cell using 40 µm spot size, at 5 Hz and ~2.5 j/cm^2 fluence with a 40 s dwell time. Helium was used as a

carrier gas in both instruments and was mixed with argon from a desolvating nebulizer. The following masses were measured: ^{139}La, ^{140}Ce,^{141}Pr, ^{146}Nd, ^{149}Sm, ^{153}Eu, ^{157}Gd, ^{163}Dy, ^{165}Ho, ^{167}Er, ^{172}Yb and ^{175}Lu and were normalized to ^{44}Ca assuming 39.7% Ca in the apatite mineral. Terbium and thulium were not analysed. NIST612, using values from Jochum et al. (2011), was used as a standard and analysed four times per ten samples. The reproducibility of NIST612 within each analytical session was better than 10% for each mass measured for both instruments. During LA-ICP-MS analysis, Ba oxides interfere with Eu and light (LREE) oxides interfere with the heavy (HREE) oxides (Kent and Ungerer, 2005). The rate of Ba- and LREE-oxide formation is similar to, or less than, that of Th- and U-oxides, as confirmed in a separate analytical session, and these oxides monitored during analysis were <0.3% for UO/U and <0.6% ThO/Th. To assess Ba-oxide interference on Eu measurements, the Ba content was measured in samples analysed at NIGL.

Measured REE abundances were normalized against Post Archaean Average Shale (PAAS: Taylor and McLennan, 1985) and marked with subscript "N" after the element symbol. Cerium anomalies were calculated (i) arithmetically as the half sum of neighboring elements: $Ce/Ce^* = Ce_N/(0.5Pr_N + 0.5La_N)$ (Bau and Dulski, 1996); and (ii) geometrically by extrapolating back from Pr and Nd abundances assuming that ratio between neighboring elements remains constant: $Ce/Ce^* = Ce_N/[Pr_N^*(Pr_N/Nd_N)]$ (McLennan, 1989). Also the La anomaly was calculated geometrically using equation: $La/La^* = La_N/[Pr_N^*(Pr_N/Nd_N)^2]$ (McLennan, 1989). This approach was selected to avoid La anomaly interference on Ce anomaly assessment. Praseodymium and Nd were selected as references because there is no known mechanism for Pr and Nd fractionation (Bau and Dulski, 1996). Geometrically calculated Ce and La anomalies are used throughout the paper, if not stated otherwise. The Eu, Pr and Y anomalies were calculated as the half sum of neighboring elements: $Eu/Eu^* = Eu_N/((Sm_N + Gd_N)/2)$, $Pr/Pr^* = Pr_N/(0.5Ce_N + 0.5Nd_N)$, $Y/Y^* = Y_N/((Dy_N + Ho_N)/2)$ (Bau and Dulski, 1996 and Byrne and Sholkovitz, 1996).

4. Results

4.1. XRD, XRF and petrography

Studied samples are coarse-grained gritstones and sandstones composed of sub-rounded to rounded quartz (chert)-feldspar-schist grains (Fig. 3). Samples AL05-P04, AL05-P06 and AL05-P07 are rich in pyrite and pyrrhotite, up to 35 wt% of the crystalline phases (Table 1), whereas the quartz content varies from 33 to 34 wt% in pyritic gritstones to ca. 70 wt% in typical gritstone and sandstone lithologies (Table 1). The P_2O_5content in the studied samples varies between 1.5 and 3.9 wt% and is mainly represented by carbonate-fluorapatite (Table 1, Fig. 4).

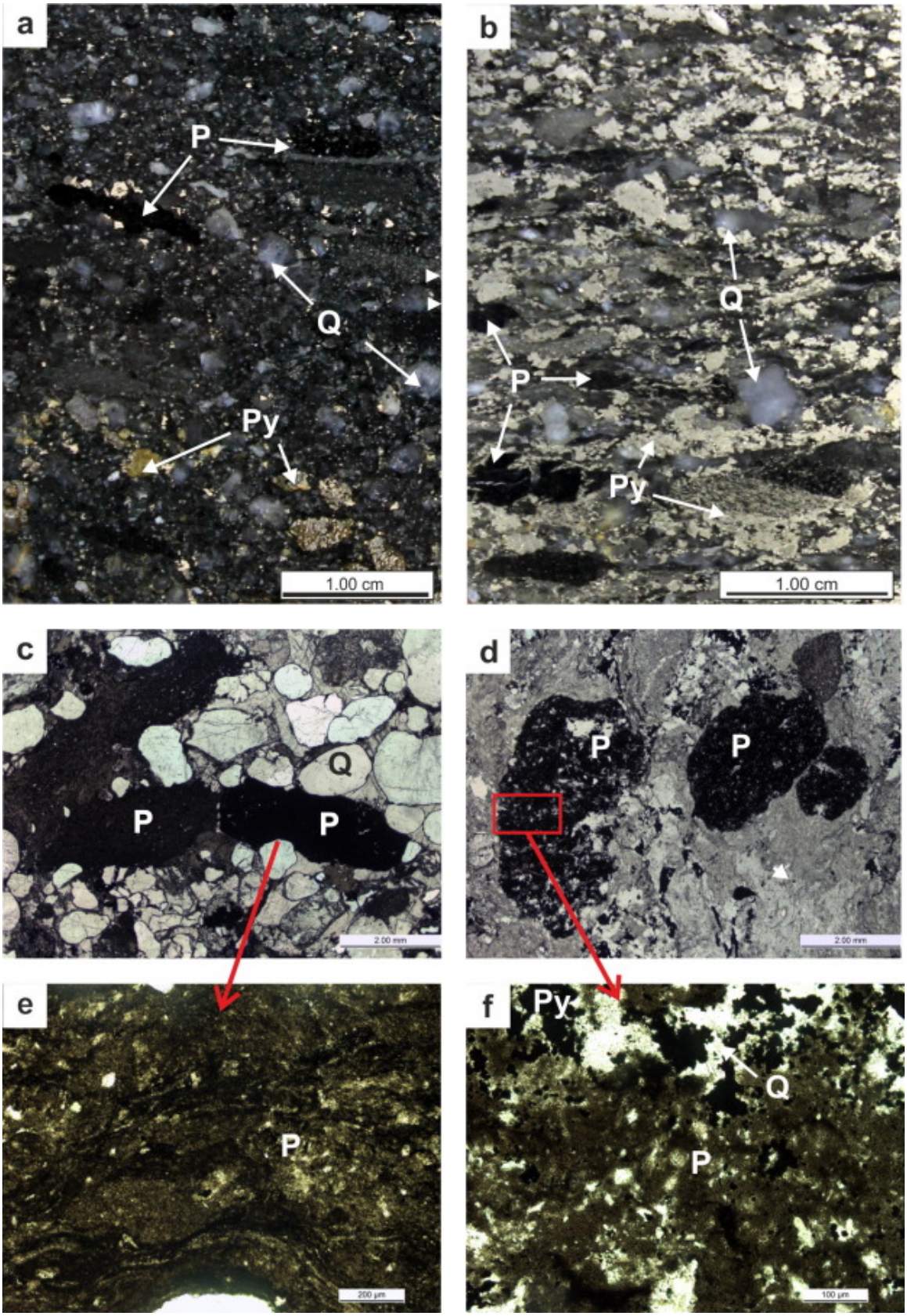

Fig. 3. Optical images of the polished slabs from samples (a) AL05-P04 and (b) AL05-P07. Optical microscope images of phosphatic grains in parallel nicols in thin-sections from samples AL05-P05 (c, e) and AL05-P06 (d, f). Note the soft deformation and banding of the lamina in organic-rich phosphatic grain (e). Legend: P – phosphatic grain Q – quartz, Py – pyrite.

Table 1.

Whole-rock mineral composition and P_2O_5 concentration in studied samples, wt%. tr – trace amount < 0.5 wt%.

Phase	AL05-P02	AL05-P03	AL05-P04	AL05-P06	AL05-P07
Quartz	72.6	34.7	73.6	46.4	33.8
K-feldspar	1.9	2.7	3.3	2.7	2.8
Plagioclase	2.9	6.2	7.9	8.5	9.4
Phlogopite	2.2	4.7	1.5	1.5	0.8
Chlorite	8.4	2.9	8.8	2.7	3.3
Apatite	4.5	9.2	3.5	4.1	5.6
Calcite	6.9	3.9	tr.	5.3	7.7
Dolomite		tr.			
Pyrite	0.6	34.0	0.5	28.1	35.2
Pyrrhotite	tr.	1.2	1.2	0.8	0.9
Jarosite		tr.			
P_2O_5	2.07	3.90	1.59	1.76	2.31

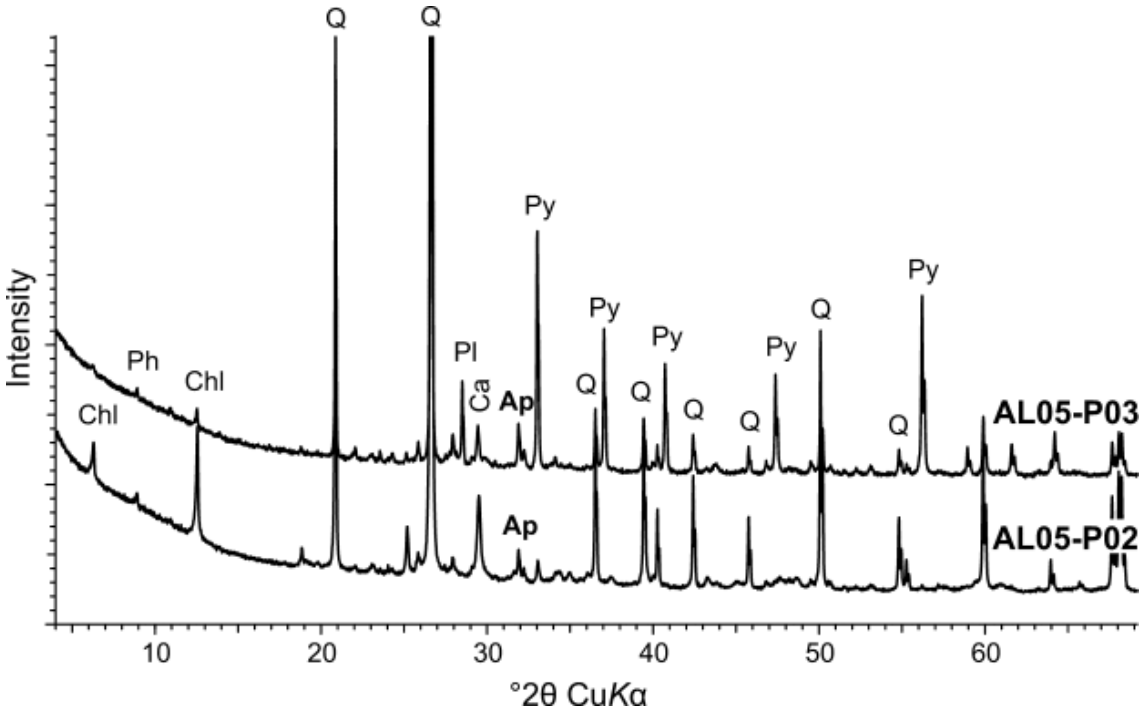

Fig. 4. Representative whole-rock X-ray diffraction patterns of Pilgujärgi SF P-rich coarse-grained sediments. Legend: Chl – chlorite, Ph – phlogopite, Q – quartz, Pl – plagioclase, Ca – calcite, Ap – apatite, Py – pyrite.

Phosphatic grains in the studied gritstone–sandstone samples are typically tabular elongated and sub-angular to rounded (Fig. 3), but some are well-rounded and spherical (Fig. 3d). The typical size of phosphatic grains varies between 0.2 and 1.0 mm, but some grains are up to 5 mm in diameter. The phosphatic grains can be subdivided into four petrographically defined types (Fig. 5) that can co-occur in samples (Fig. 6). These are:

A. angular to sub-angular grains of massive, impurity-free, sub-micrometer size apatite crystal aggregates (AL05-PO4 and AL05-PO5);

B. elongated and sub-rounded grains of apatite cemented siltstone-shale (composed of quartz, feldspar, and mica) or silicifed dolostone (chert) (AL05-PO2 and AL05-PO5);

C. sub-angular to rounded grains of apatite aggregates with abundant quartz and feldspar, possibly a transitional type between A and B type grains (AL05-PO2, AL05-PO4, AL05-PO5 and AL05-PO6);

D. sub-angular and angular apatite crystal aggregates with abundant pyrite (AL05-PO6).

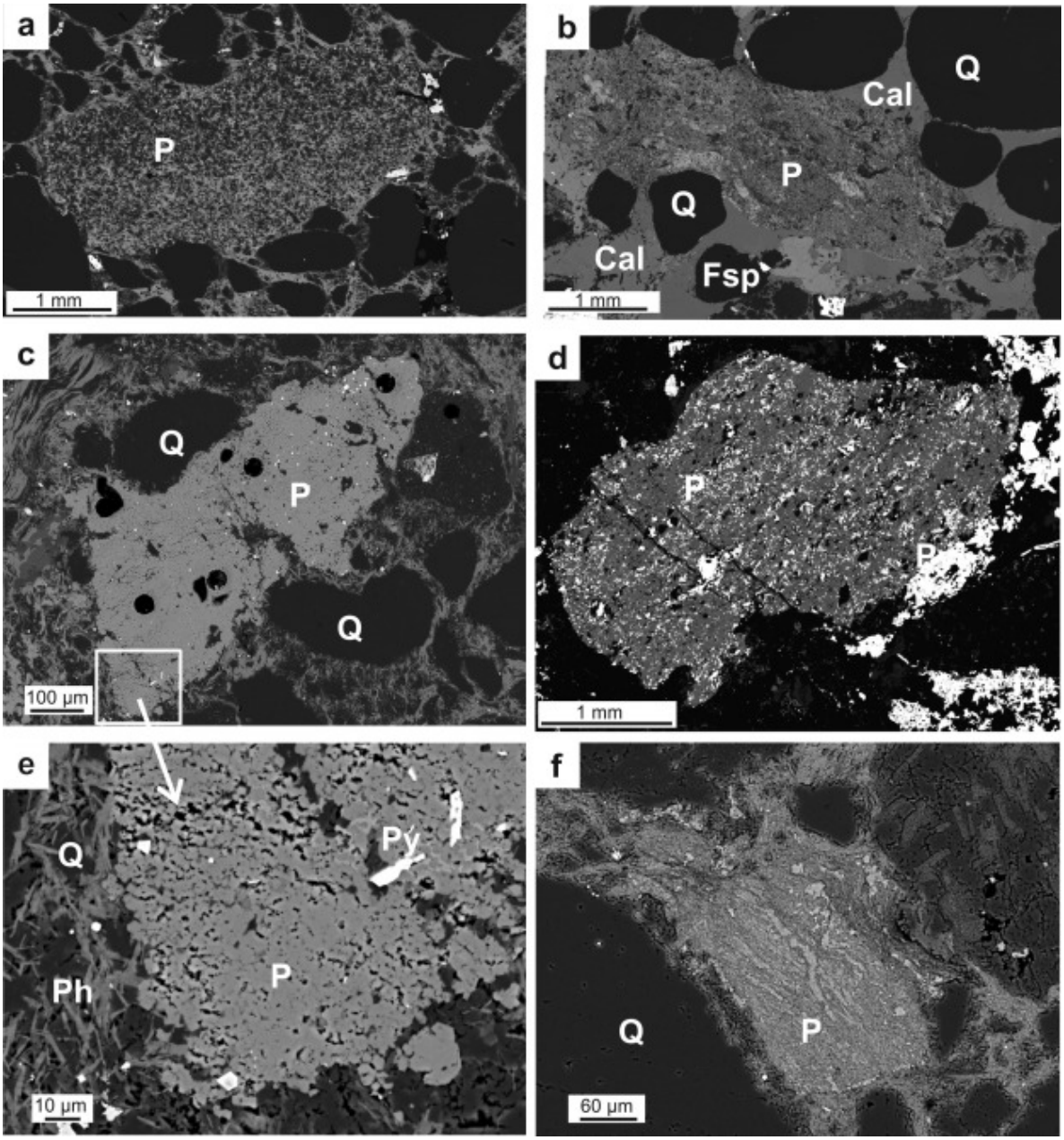

Fig. 5. SEM back-scattered electron images of phosphatic grains. (a) Elongated and subrounded grain of apatite cemented quartz-feldspar-mica/chlorite siltstone and shale (Type B, AL05-P04), (b) sub-angular phosphatic grain with abundant quartz and feldspar (Type C, AL05-P05), (c) angular to sub-angular phosphatic grain consisting of massive apatite crystal aggregate (Type A, AL05-P04), (d) apatite aggregate with abundant pyrite (Type D, AL05-P06), (e) magnified detail of the phosphatic grain in panel (c), (f) rare laminated phosphatic grain, light laminae are rich in apatite, dark laminae are clay (AL05-P04). Legend: P – phosphatic grain, Q – quartz, Ph – phlogopite, Py – pyrite, Cal – calcite, Fsp – feldspar.

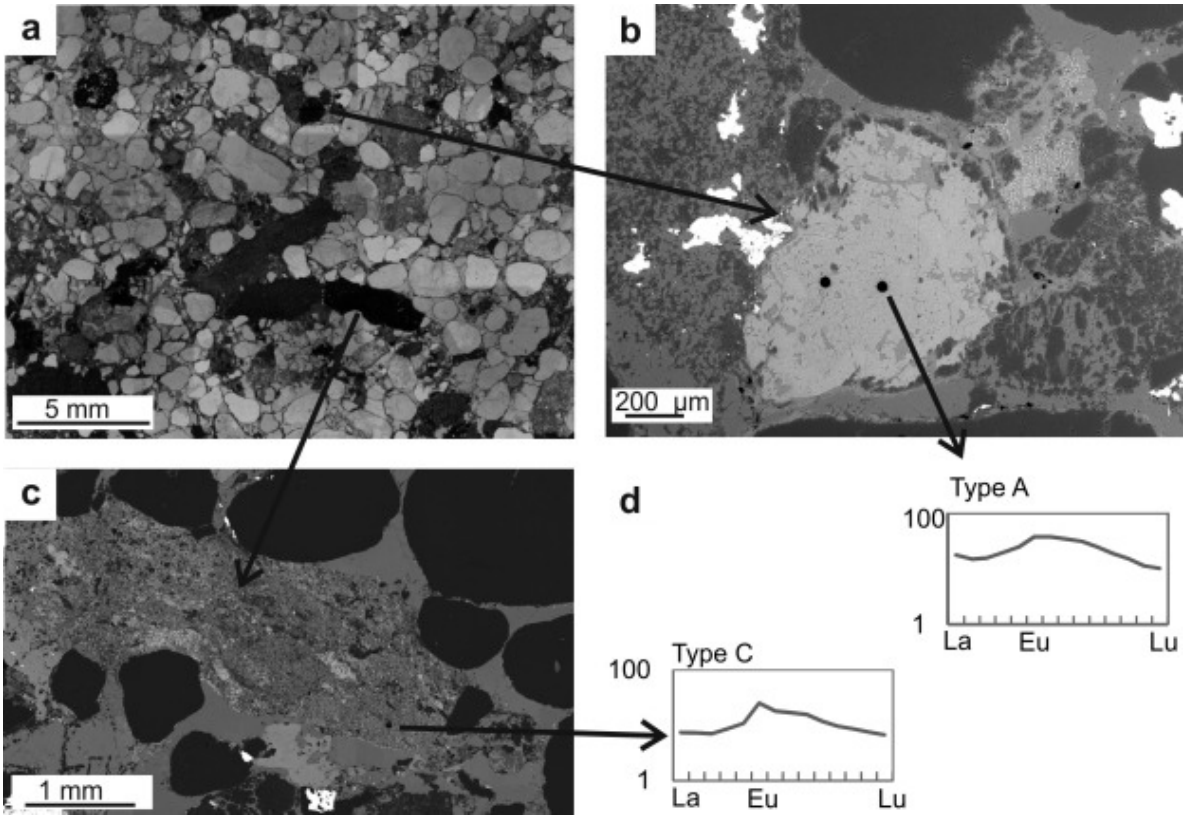

Fig. 6. Co-existing phosphatic grains of type A and C in sample AL05-P05, which contains apatite with different REE patterns. (a) Optical microscope image of sample AL05-P05, (b and c) BSE images of phosphatic grains and (d) REE patterns of apatite in type A and C grains.

Rare laminated shale grains rich in apatite were also found (Fig. 5f). Some organic rich phosphatic mudstone grains interpreted as rip-up mud clasts show soft-deformation features (e.g. bending around quartz grains, concave-convex contacts, Fig. 5b and c). This indicates that these particles were not lithified (rigid) during deposition. Apatite also occurs as fine-crystalline anhedral aggregates with uniformly fine crystallite size (<0.3 µm, Fig. 7a–c). Agglomerated 2–3 µm size spherical apatite aggregates composed of radially growing apatite crystallites were found in one phosphatic grain in sample AL05-P05 (Fig. 7d). Fine-grained granular texture of apatite aggregates and textural relationships between apatite cement and quartz, feldspar and mica grains in type B, C and D phosphatic grains suggest rapid early diagenetic precipitation of apatite from interstitial fluid supersaturated with respect to phosphate in pore space of the pre-compacted sediment. Massive apatitic aggregates in type A grains resulted most probably from recrystallization of earlier cements or represent remnants of discrete phosphatic lenses/layers precipitated within the upper unconsolidated portion of the sediment column.

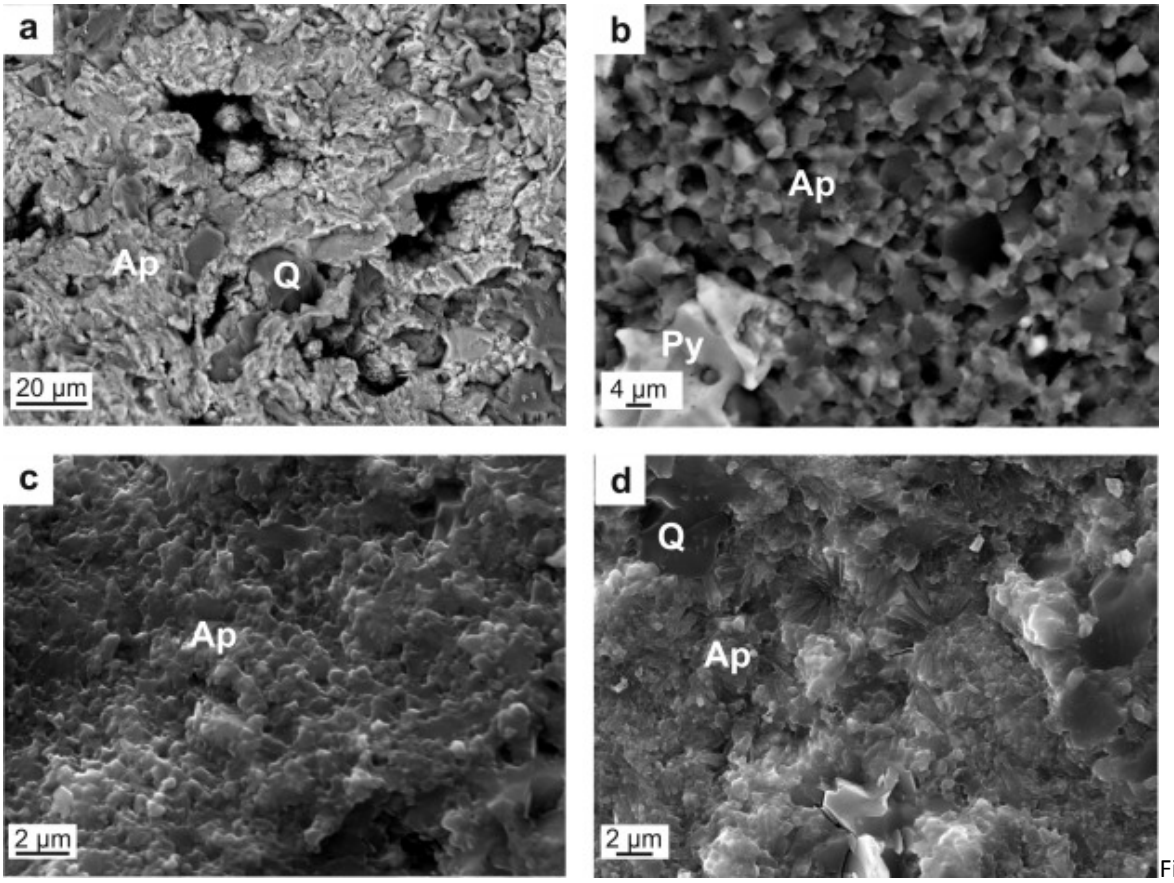

Fig. 7. SEM images of phosphatic grains on fractured surface. (a) Sample ALO5-P06, (b) AL05-P06, (c) AL05-P05 and (d) flower-like apatite aggregates in sample A05-P05. Pt-coated sections were imaged using a backscattered electron detector (a and b) and secondary electron detector (c and d).

Pyrite in sulfide-rich samples (e.g. AL05-P06, Table 1) occurs in gritstone matrix as aggregates of euhedral pyrite crystals (Fig. 8a), where the pyrite crystals show weak zoning (Fig. 8b). In phosphatic grains, pyrite occurs as xenomorphic–dendritic aggregates of fine/disseminated pyrite crystallites between the massive apatite (Fig. 8c and d). The pyritic areas in D-type phosphatic grains show indistinct banding-lamination (Fig. 5d). Pore-filling euhedral pyrite aggregates are possibly related to the hydrothermal activity initiated by intrusion of ferropicritic igneous rocks and synvolcanic Ni–Cu mineralization in the Pilgujärvi SF (Melezhik and Sturt, 1994), whereas the pyrite within phosphatic grains might be an early diagenetic sedimentary pyrite. Glenn and Arthur (1988) have shown co-precipitation of pyrite and apatite in modern shelf phosphorites off the Peruvian coast, while pyrite precipitation continues beyond that of apatite and it may replace the apatite, or infill remaining pore space after partial interstitial apatite cementation.

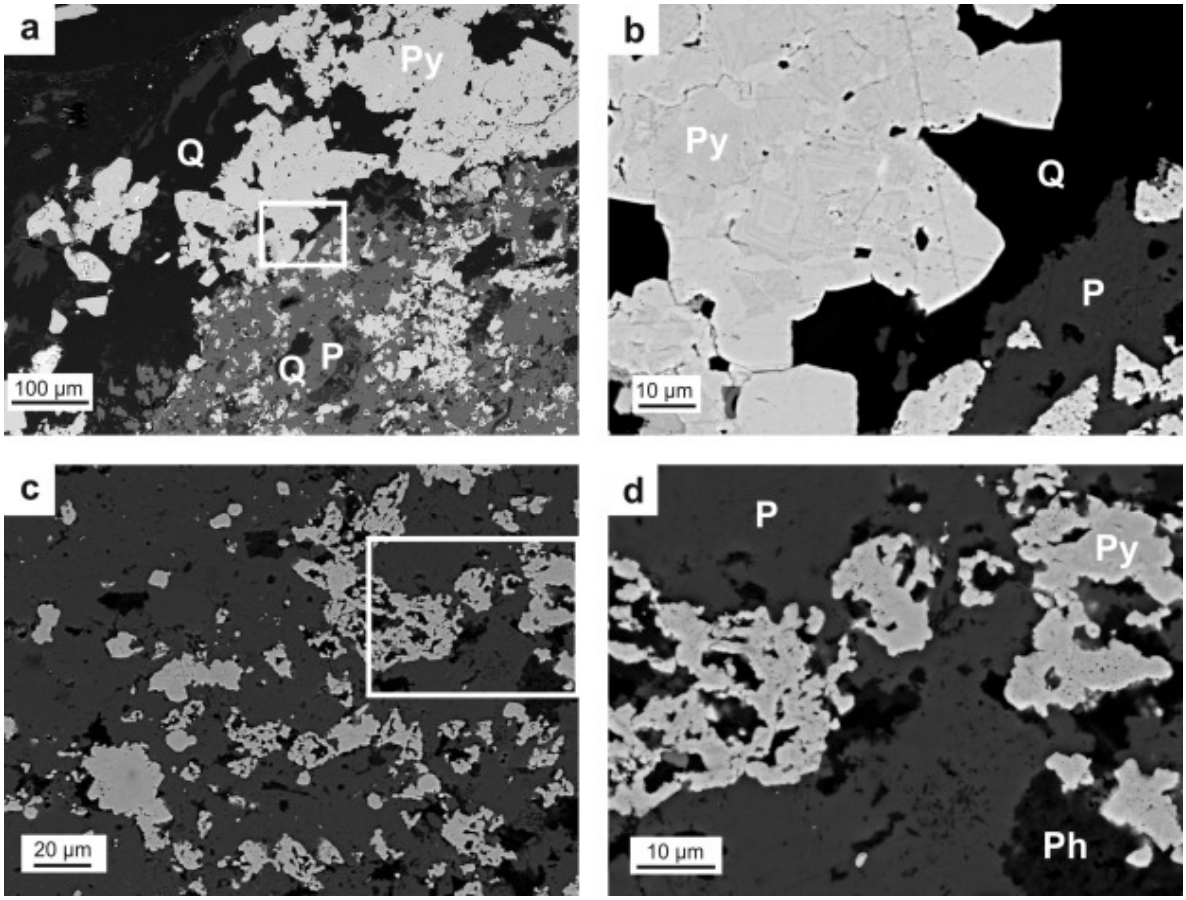

Fig. 8. SEM back-scattered electron images showing pyrite in sulfide-rich sample AL05-P06. (a) Contact between phosphatic grain (lower right corner) and pore-filling massive pyrite aggregate. (b) Close-up (white rectangle in (a) of massive pyrite aggregate with zoned euhedral pyrite crystals. (c) Dendritic-xenomorphic pyrite aggregates embedded in apatite within the phosphatic grain. (d) Close-up (white rectangle in (c)) of the pyrite aggregates. P – Apatite, Py – pyrite, Ph – phlogopite, Q – quartz.

4.2. Rare Earth Element composition of phosphatic grains

The REE analyses of apatite (Table 2; Fig. 6 and Fig. 9) indicate a systematic variance of REE patterns in different petrographic types of phosphatic grains. The PAAS normalized REE patterns of grains comprising massive apatite crystal aggregates (type A, Fig. 10a) are characterized typically by a smooth bell-shape pattern with elevated mid (M)-REEs (Gd_N to Er_N), and depleted LREEs (La_N to Sm_N) and even more depleted HREEs (Er_N to Lu_N). The average La_N/Sm_N ratio of this type is 0.5 whereas the average Gd_N/Er_N and Er_N/Lu_N ratios are 2.4. Apatite REE patterns of type B grains (where apatite occurs as a cementing matrix) are flatter than type A (Fig. 10b), but also show enrichment in MREEs with a distinct, positive Eu anomaly and in some spots a weak, positive Ce anomaly. Some apatite REE patterns of type B grains are similar to type A patterns with clearly emerging MREE enrichment. The La_N/Sm_N, Gd_N/Er_N and Er_N/Lu_N values of type B are 0.7, 1.6 and 1.8, respectively. Grains of type C, that are petrographically transitional between types A and B, have also mixed/intermediate REE patterns with characteristics of A and B types (Fig. 10c). The average La_N/Sm_N, Gd_N/Er_N and Er_N/Lu_N values of apatite in type C grains are 0.6, 2.0 and 1.8, respectively. In contrast, the REE patterns of the phosphatic grains rich in pyrite (type D)

have flat LREEs and MREEs, but show slightly depleted HREEs with an average La_N/Sm_N of 1, Gd_N/Er_N 1.1 and Er_N/Lu_N ratio of 1.4.

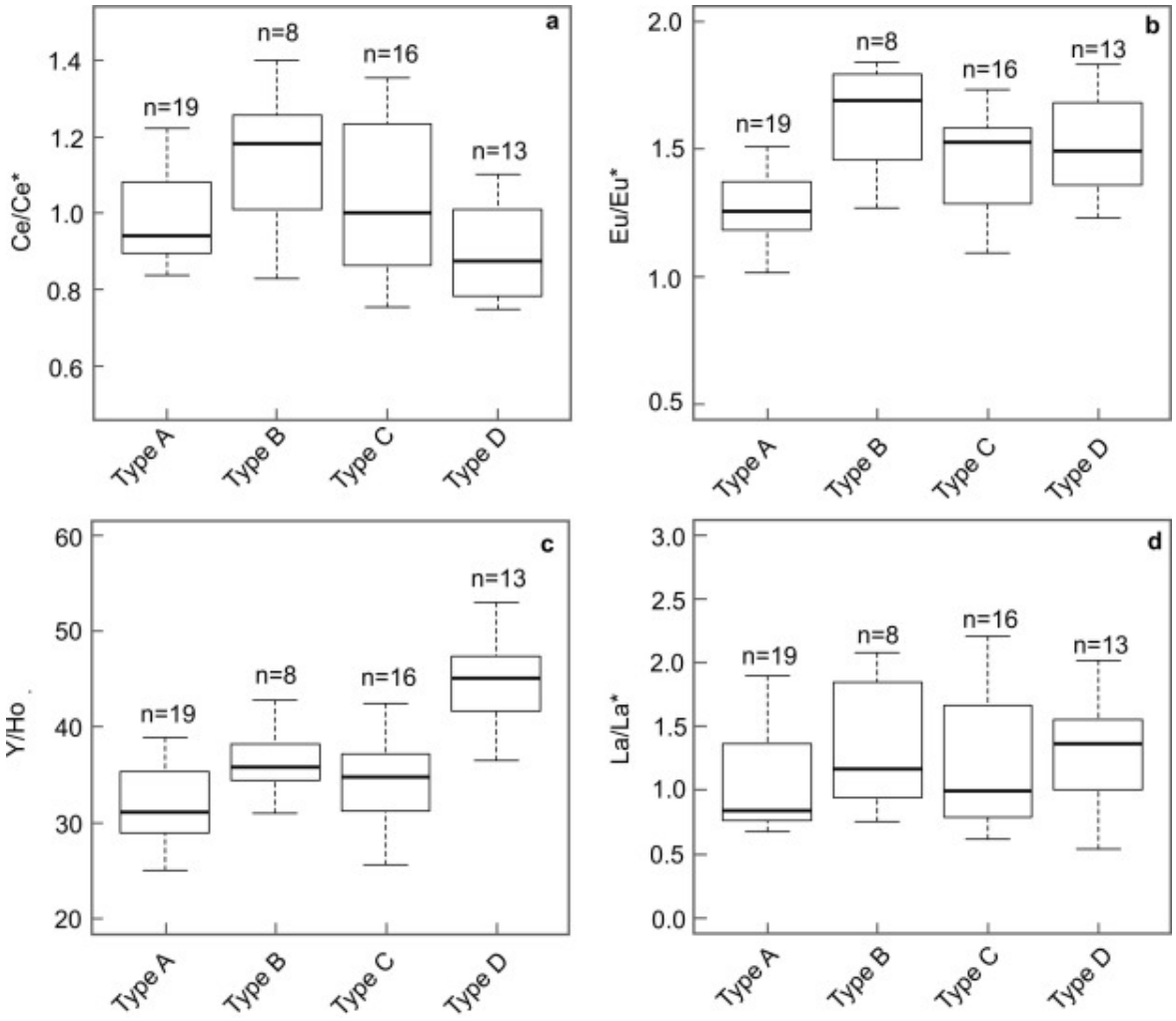

Fig. 9. (a) Ce anomaly, (b) Eu anomaly, (c) Y/Ho ratio variations and (d) La anomaly in apatite in each petrographic type.

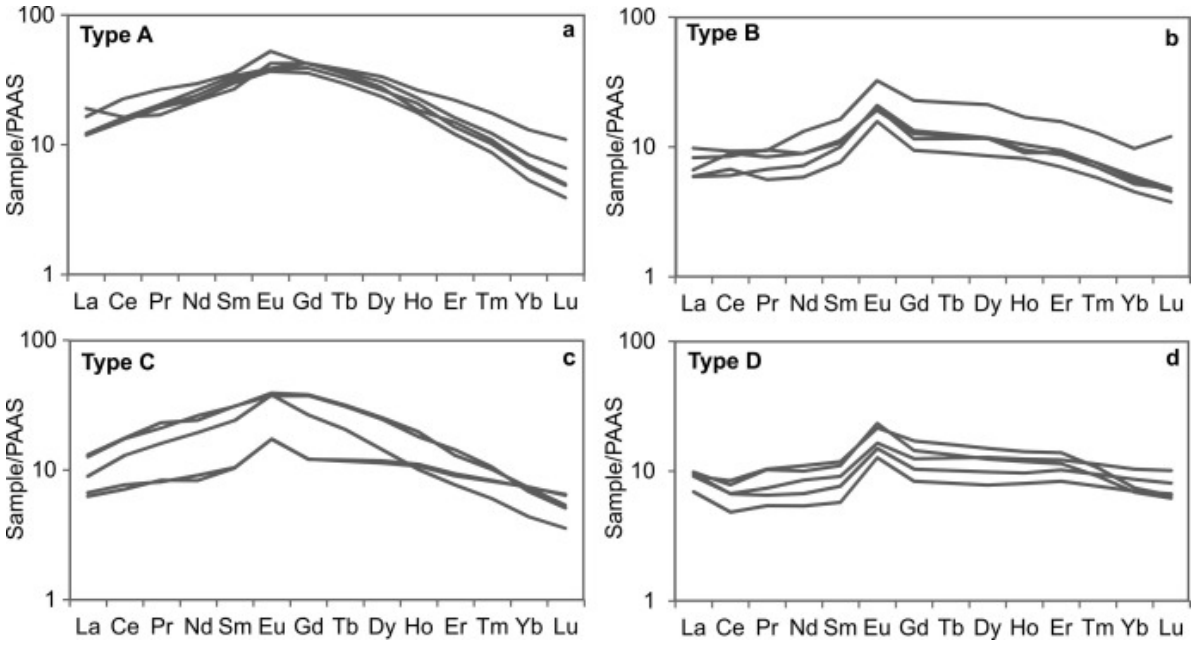

Fig. 10. Post-Archean Australian Shale (PAAS) normalized REE patterns of apatite in phosphatic grains of different petrographic types. Five representative REE patterns were selected from each type. (a) type A, (b) type B, (c) type C and (d) type D phosphatic grains.

Values of La/La* fluctuate from negative to positive in all petrographic types and show no preference to a specific type (Fig. 9d and Table 2). The lowest average La/La* value is in type A (1.1) and is slightly higher in type C (1.2). Types B and D have somewhat higher average La/La*: 1.3 and 1.4, respectively. Similarly, the Ce anomaly fluctuates from slightly negative to positive values within each petrographic type (Fig. 9a). The lowest average Ce/Ce* value is in type D (0.9) and highest in type B (1.1). Negative Ce anomalies in type D grains can be defined as true anomalies using the Bau and Dulski (1996) cross plot of arithmetically calculated Ce/Ce* and Pr/Pr* values (Fig. 11c) though some of the negative Ce/Ce* values in type A and C grains are evidently due to positive La anomaly.

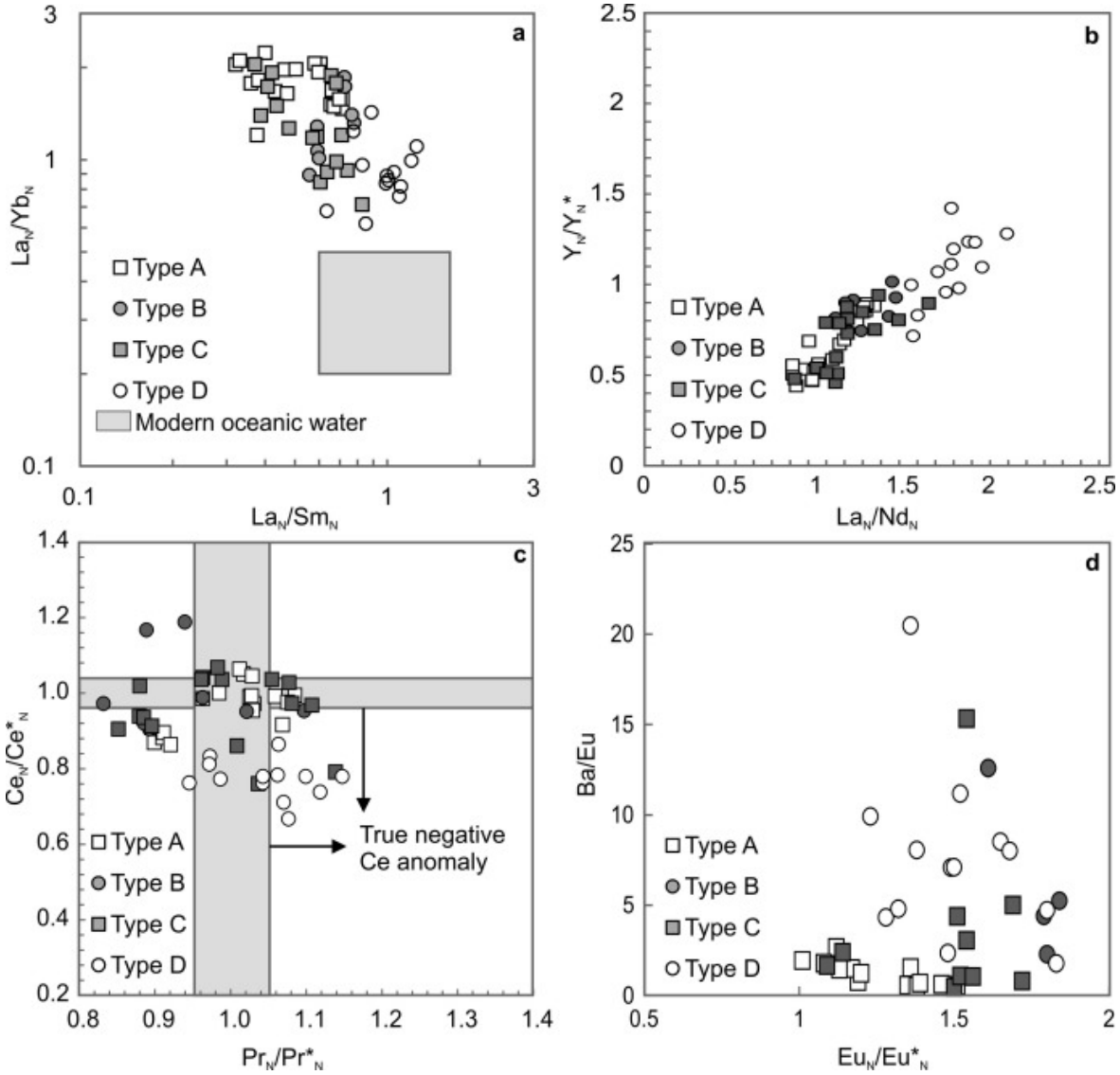

Fig. 11. Cross plots of REE ratios. (a) La_N/Yb_N and La_N/Sm_N variation. Elevated La_N/Yb_N values may indicate early digenetic LREE enrichment. Modern seawater values are from Reynard et al. (1999). (b) Y/Y^* and La_N/Nd_N variation. Lowering trend of both ratios from type D to type A and C can be explained by digenetic recrystallization (Shields and Stille, 2001). (c) Ce vs. Pr anomaly: gray areas denote no or uncertain Ce anomaly (Bau and Dulski, 1996). Note that both anomalies are calculated as the half sum of neighboring elements. (d) Cross plot of Ba/Eu and Eu anomaly shows no correlation, indicating that Eu anomalies are not significantly affected by Ba-oxide interference. All ratios are given using PAAS normalized REE abundances, except Ba/Eu (d) in which measured abundances are used.

The Eu anomaly is positive in all types, but shows slight difference between individual types (Fig. 9b). The lowest average of Eu/Eu^* is in type A (1.3) whereas the average Eu/Eu^* in type B is 1.6 and ca. 1.5 in C and D types. Positive Eu anomaly can be caused by Ba-oxide interference. However, the Ba content in measured samples is in average 87 ppm (maximum value 307 ppm, Table 2). The Ba/Eu values in the samples are <100, suggesting at oxide formation rates <0.6% an overestimate of less than 10%. Moreover, there is no correlation between Eu/Ba and the Eu/Eu^* values (Fig. 11d) indicating that Eu anomalies do not appear to be significantly affected by oxide interference.

There is a clear difference in Y/Ho ratio between petrographic types (Fig. 9c). Types A, B and C show average Y/Ho values of 32, 36 and 34, respectively. However, the Y/Ho average of 46 in type D is distinctly higher compared to other types. The Y anomaly is absent in type A (average Y/Y^* value is 1.0) and most significant in type D (1.7). In types B and C the Y anomaly is 1.2 and 1.1, respectively.

5. Discussion

The data show that apatite-rich grains in the Pilgujärvi SF representing different petrographic types have distinct REE compositions. This suggests either diverse origin (formation environments) and/or different grades of secondary alteration. However, it is important to note that different petrographic types with distinct REE patterns co-occur in the same samples (Fig. 6), suggesting that both petrographic appearance and variations in REE patterns reflect the depositional/diagenetic settings prior to reworking of the Pilgujärvi SF phosphorites, and that the REE signal is not, at least significantly, altered by the greenschist-facies metamorphic overprint of the Pechenga Greenstone Belt sequence.

5.1. Preservation of the REE signal

The REE composition of authigenic sedimentary apatite has been shown to reflect the water composition at the time and location of its precipitation (e.g. Piper and Bau, 2013). However, it is commonly considered that apatite takes up the REEs by surface adsorption during early diagenesis and, most importantly, by structural substitution for Ca in the apatite lattice during late diagenetic recrystallization (Reynard et al., 1999).

Bell shaped REE patterns of the A-type phosphatic grains are usually interpreted as characteristic for MREE enrichment during the late diagenetic and hydrothermal recrystallization process. The MREEs preferentially substitute for Ca in the apatite crystal lattice due to similar ionic radii (Morad and Felitsyn, 2001) and such preferential substitution is expected to progress with late diagenetic recrystallization. The early diagenetic adsorption of REEs on crystal surfaces should lead to LREE enrichment (Reynard et al., 1999). However, bell-shaped MREE enriched patterns of A, C and some B type grains can also result from apatite precipitation in depositional settings influenced by Fe(Mn)-oxyhydroxide redox-cycling and related adsorption-desorption of phosphate and REEs (e.g. Jarvis et al., 1994 and Haley et al., 2004). Haley et al. (2004)demonstrated the occurrence of bell-shaped pore water REE profiles in a diagenetic Fe-oxide reduction zone in modern sediments on the Californian margin reflected the signature of REEs adsorbed onto the Fe-oxides in the water column. Adsorbed REEs and phosphate are liberated to pore water during burial and reductive dissolution of freshly deposited Fe(Mn)-oxyhydroxides below the suboxic–anoxic redox boundary, resulting in MREE enriched pore water (Haley et al., 2004). Apatite precipitating in this Fe(Mn)-oxide reduction zone would show MREE enrichment and the highest average total REE concentrations, such as is seen in Pilgujärvi SF type A-grains (Fig. 10). The MREE enrichment is less pronounced in B-type grains and nearly absent in D-type; the latter being characterized by positive Eu anomalies and flat MREE and HREE patterns. The La_N/Sm_N ratios fall within the range of modern seawater in B- and D-type phosphatic grains, whereas in A- and C-types the La_N/Sm_N ratios are mostly lower than typical modern seawater values (Fig. 11a). Somewhat elevated La_N/Yb_N ratios in all

petrographic types compared to modern seawater values may indicate the adsorption of LREEs on crystal surfaces, possibly during early diagenesis. Apatite in D-type grains seems to have preserved the most seawater-like pattern as shown by La_N/Yb_N and La_N/Sm_N ratios.

Phosphatic grains of the Pilgujärvi SF are not *in situ* but eroded, transported and re-deposited (Akhmedov and Krupenik, 1990 and Melezhik and Sturt, 1998; Bekasova, 1985) implying a possible weathering imprint on apatite REE composition. Shields and Stille (2001) have proposed that REEs tend to be released during weathering because surface waters have low concentration of REEs compared to apatite. During weathering La, Gd and Y should be preferentially retained in apatite due to a tetrad effect (Bau et al., 1996). As a consequence, Y/Y^* and La_N/Nd_N should increase during weathering (Shields and Stille, 2001) resulting in a positive correlation between Y anomaly and La_N/Nd_N. In Pilgujärvi SF samples a positive covariance between Y/Y^* and La_N/Nd_N is particularly evident in A-type grains (Fig. 11b). However, diagenetic recrystallization processes can also produce a positive Y/Y^* versus La_N/Nd_N relationship (Reynard et al., 1999). Moreover, the Pilgujärvi SF P-rich gritstone contain well-preserved clasts rich in sedimentary pyrite (Fig. 5), which suggests that clasts were not influenced, at least significantly, by weathering. Nevertheless, some grains, including the ones that have preserved pyrite intact in their interior, have thin Fe-oxide coatings (Fig. 12) and decreasing pyrite abundance gradients toward the edge of the grains (Lepland et al., 2013), implying either reworking in surface environments or influence of percolating meteoric waters. This means that great caution needs to be taken when interpreting REE patterns and anomalies, especially concerning La, Gd and Y. Therefore, the Ce anomaly for Pilgujärvi apatite was calculated geometrically using Pr and Nd to avoid the potentially anomalous behavior of La in the calculations.

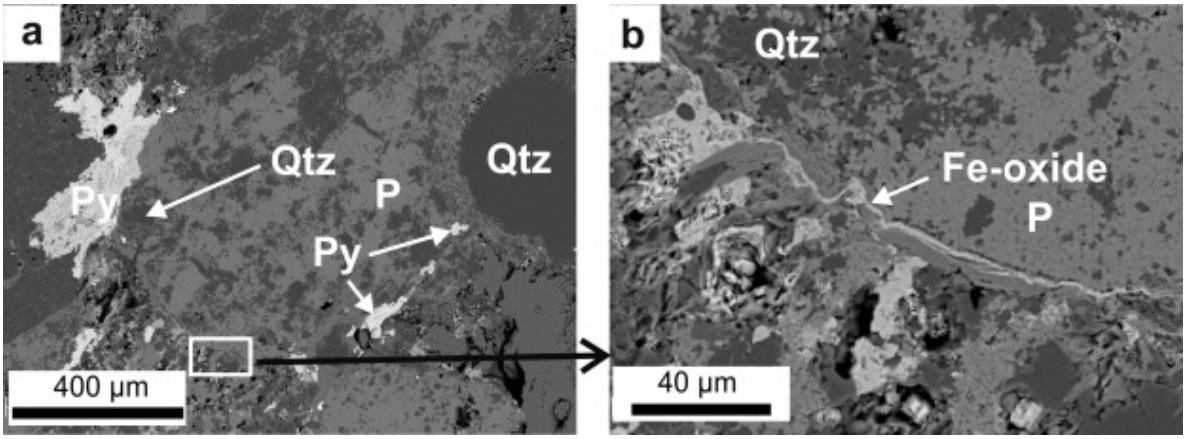

Fig. 12. Fe-oxide coating on the phosphatic grain with intact pyrite. Q – quartz, P – phosphate, Py – pyrite. (a) An overview image and (b) close-up of the Fe-oxide coating.

5.2. Environmental interpretation

The REE patterns of authigenic apatite are widely used to infer the redox chemistry of ancient oceans (e.g. Joosu et al., 2015 and Wright et al., 1987). However, biologically precipitated apatite is a thermodynamically unstable, hydroxyapatite-like, poorly crystalline phase (Neary et al., 2011) that is readily recrystallized during diagenesis (Trueman, 2013). Consequently, biogenic hydroxylapatite has been shown to be an ambiguous carrier of information about primary redox conditions, specifically due to recrystallization and

adsorption effects (e.g. Herwartz et al., 2013). In contrast, the sedimentary carbonate-fluor apatite (Knudsen and Gunter, 2002) is a thermodynamically stable apatite phase in solutions with elevated bi-carbonate anion activity, such as seawater (Jahnke, 1984). Therefore, in the absence of a thermodynamic driver for recrystallization, the sedimentary apatite could be considered as a stable phase and the REE composition of authigenic sedimentary apatite may record the ambient water conditions at the time and location of precipitation (Piper and Bau, 2013).

The Ce anomaly in apatite in particular is considered to be a proxy for sedimentary environment oxidation state (Liu et al., 1988, Slack et al., 2007, Bekker et al., 2010 and Ling et al., 2013). A Ce anomaly should not be present in authigenic sedimentary phases when the water column was fully reducing and is absent in the sedimentary rock record prior to the GOE at ca. 2.3 Ga (Planavsky et al., 2010). In oxygenated and mixed modern oceans, Ce is removed from the water column by Fe–Mn oxyhydroxides, giving a negative Ce anomaly. In stratified water-bodies with well-developed redoxclines (e.g. the Black Sea), negative Ce anomalies become increasingly negative with depth until reaching the redoxcline, where it sharply diminishes due to reduction of Ce^{4+} to a soluble Ce^{3+} as the environment becomes anoxic and euxinic (Schijf et al., 1991). Ce anomaly reflecting the redox status of the depositional and/or diagenetic environment is recorded in early diagenetic authigenic minerals such as Ca-phosphate and calcite/aragonite precipitating in equilibrium with the seawater or pore water, which has been shown in modern settings (Wright et al., 1987, Arning et al., 2009 and Piper and Bau, 2013). The Ce anomalies recorded in the Pilgujärvi SF fluctuate from slightly negative to positive in all petrographic types (Fig. 9a), though the Ce/Ce^*values are mostly negative in D-type grains. Variable Ce anomaly values thus suggest that the apatite precipitation and formation of cements occurred close to the fluctuating redox boundary within the shallow sediment depth below the sediment–water interface. Negative values indicate that the water column and/or pore water was (sub)oxic resulting in preservation of Ce fractionation generated in oxic waters. Positive values are probably the effect of a change in redox boundary that resulted in Ce remobilization from dissolving Fe–Mn-oxyhydroxides under anoxic conditions and in increased Ce concentrations in pore waters or water column. Wright et al. (1987) has shown that while Ce/Ce^* values of authigenic apatite are strongly negative in deep ocean sediments, apatite formed in high primary productivity regions on modern continental shelves (Peru, Namibia) is characterized by Ce/Ce^* values that are positive or only slightly negative, reflecting a suboxic-to-anoxic state of the sea-bottom environments.

The Eu anomaly in the studied samples is positive in all petrographic types, varying from approximately 1.0–1.84 (Fig. 9b). Eu does not fractionate under normal low temperature surface conditions. However, in extremely reducing and/or high temperature (>200 °C) environments it is reduced to mobile Eu^{2+}. Europium anomalies are therefore commonly observed in hydrothermal fluids and venting site sediments and even in shells of organisms inhabiting these sites (Bau et al., 2010). These anomalies can be positive (Michard et al., 1993 and Bau et al., 2010) as well as negative (Bach et al., 2003). Unlike the Ce/Ce^*, the Eu anomaly recorded in authigenic apatite is considered to be a stable tracer that does not change during diagenesis (Mazumdar et al., 1999 and Shields and Stille, 2001). Consequently, the positive Eu/Eu^* values in Pilgujärvi SF phosphatic grains are attributed to a hydrothermal influence. The Pilgujärvi SF comprises numerous mafic-ultramafic sills and minor lava flows and hosts the world-class Pechenga Ni–Cu-sulfide deposits. These sills and

lava flows influenced water chemistry in the vicinity of venting sites and around the margins of intrusions. Intriguingly, the variable Eu anomaly in Pilgujärvi SF apatitic grains may reflect varying proximities to the venting sites and/or a changing influence of the magmatic/hydrothermal discharges during deposition: the P-rich sediments with the higher Eu anomaly values would have been deposited closer to venting sites or during higher magmatic activity and those with lower values would have precipitated at some distance to vents or during periods of lower magmatic activity (e.g.Bau et al., 2010).

A hydrothermal influence is further supported by low Y/Ho ratios in the A-, B- and C-type apatite grains. The Y/Ho ratio in igneous rocks and in hydrothermal fluids is close to the chondritic value of 28 (Bau et al., 1996 and Bau and Dulski, 1999), whereas seawater and marine chemical sediments typically have Y/Ho values > 50 (Nozaki et al., 1997). The latter is due to seawater Ho being more reactive towards Fe–Mn particles than Y (Bau and Dulski, 1994). However, the Y/Ho molar ratio is also affected by redox cycling and the Ho that was preferentially adsorbed with respect to Y on Fe- and Mn-oxyhydroxides in oxygenated (surface)water can be released in the anoxic brine of the stratified water column and thus result in lower Y/Ho ratios (Bau et al., 1997). Nevertheless, the elevated Y/Ho values of the apatite in type D grains (average 46) suggest phosphate precipitation in equilibrium with a fluid whose REE and Y composition was rather similar to modern oxygenated seawater. This interpretation is further supported by the Ce anomaly values that are mostly negative in D-type grains, suggesting deposition in a oxygenated environment.

The variation in petrographic appearance and in REE composition of the phosphatic grains may reflect a different degree of diagenetic/hydrothermal alteration. This scenario implies that the A-type grains, composed of mostly pure apatite and characterized with MREE enriched bell-shaped REE patterns, are late, diagenetically or hydrothermally recrystallized phosphate aggregates. In this case the C- and B-type grains are progressively less recrystallized/altered aggregates and the D-type grains are the most pristine.

Irrespective of the exact reason for the petrographic and REE variations, we suggest that apatite in type D grains mostly reflects original porewater conditions at the time of their formation. Weak negative Ce anomalies and high Y/Ho ratios indicate that apatite in type D grains precipitated under (sub)oxic conditions, while the positive Eu anomaly indicates a significant hydrothermal influence on seawater in the Pechenga basin. Abundant pyrite in type D grains is consistent with the activity of sulfur-metabolizing organisms that may have controlled the P cycling and apatite precipitation in sediments represented by this type of grains.

The environmental conditions recorded in the Pilgujärvi SF apatite are similar to the phosphogenic settings in the Zaonega Formation of the Onega Basin (Lepland et al., 2014). The most pristine sedimentary diagenetic apatite in the Zaonega Formation shares similar characteristics with D-type apatite in the Pilgujärvi SF. For example the negative Ce anomaly (0.6–0.9), and positive, but variable, Eu anomaly (1.3–5.6) in the Zaonega Formation apatites suggests precipitation in suboxic conditions in unconsolidated sediment below the seawater-sediment interface (Joosu et al., 2015). These conditions are similar to modern phosphogenic areas (e.g. Arning et al., 2009) in continental shelf environments where upwelling of nutrient-rich, deep-ocean water facilitates high biological production (Föllmi, 1996). Fluctuating anoxic–suboxic redox conditions and redox-dependent microbial

processes within the sediment pore space leads to elevated phosphate concentrations resulting in apatite precipitation (Schulz and Schulz, 2005).

Positive Eu anomalies in apatite from the Pilgujärvi SF and the Zaonega Formation suggest for both units a substantial input of hydrothermal fluids during apatite formation that is consistent with the magmatically active setting of both basins (Črne et al., 2013 and Hanski et al., 2014). One point of difference between the two localities is that the Zaonega Formation phosphatic lenses and nodules formed *in situ* whereas the P-rich grains in the Pilgujärvi SF indicate some degree of sediment reworking and transport. Phosphatic grains are not widespread throughout the Pilgujärvi SF, but occur specifically in the middle of the formation in coarse-grained beds at the base of the rhythmically interbedded gritstone–sandstone–shale sequence. Lepland et al. (2013) have pointed out that gravel-size angular to rounded phosphatic grains showing soft-sediment deformation features could not have been transported over long distances and are possibly locally derived. Abundant angular–subangular phosphatic grains along with deformed mudstone clasts suggest transportation mainly by sediment gravity flows rather than in bedload. Combined, these observations support the interpretation that this part of the Pilgujärvi SF represents a proximal facies to a submarine fan complex (Akhmedov and Krupenik, 1990 and Melezhik and Sturt, 1998). The different types of phosphatic grains would have been transported downslope, analogous to resedimentation processes known to typify many slope-submarine fan settings (e.g.Postma, 1984).

6. Conclusions

The Pilgujärvi Sedimentary Formation of the Pechenga Greenstone Belt contains locally derived, resedimented phosphatic sand-to-gravel/pebble-size grains that were formed in a continental slope turbidite fan environment. Based on petrographic characteristics, the phosphatic sediment grains can be subdivided into four different types that can co-occur within the same sample. Each type has a different REE signature but all types are most compatible with apatite precipitation under early diagenetic conditions rather than being affected by late diagenetic recrystallization and/or metamorphic overprint subsequent to deposition. Grains comprising massive apatite crystal aggregates (type A) are characterized by smooth bell-shaped PAAS-normalized REE patterns, whereas type B grains, in which apatite occurs as a cementing matrix in sand-silt sized clastic sediment, show enrichment in MREEs with a distinct positive Eu anomaly. Type C grains are petrographically and chemically transitional between types A and B, whereas pyrite-rich type D grains have a relatively flat REE pattern with slightly negative Ce anomalies and positive Eu anomalies. We suggest that the REE signal in type D phosphatic grains is the best preserved and records conditions present during apatite precipitation. The slightly negative Ce anomalies in D-type grains are interpreted to reflect partial seawater oxygenation. Positive Eu/Eu^{*} values are attributed to hydrothermal venting that is consistent with the magmatically active setting of the basin. The environmental conditions of the phosphogenesis recorded in apatite in the Pilgujärvi Sedimentary Formation of the Pechenga Greenstone Belt are similar to environmental settings in the Zaonega Formation of Onega Basin, suggesting that phosphogenic events in these sedimentary basins mark the development of specific anoxic(sulfidic)–suboxic redoxclines at shallow sediment depth during the Paleoproterozoic.

Acknowledgements

We are grateful to V. Melezhik for the field guidance and discussions about the geology of the Pechenga Greenstone Belt. We are thankful to A. Bekker and anonymous reviewer whose comments significantly helped to improve the manuscript. This study was supported by Estonian Research Council project PUT969.

References

A.M. Akhmedov
Phosphorus abundance's in metasedimentary rocks of the Pechenga complex
A.A. Predovsky (Ed.), Problems of Investigation and Exploitation of Natural Resources of the North, Kola Science Centre, Apatity, Russia (1973), pp. 66–74 (in Russian)

A.M. Akhmedov, V.A. Krupenik
Turbiditic regime of sedimentation and pyrite formation in the early proterozoic pechenga basin
Sov. Geol., 11 (1990), pp. 51–60

J.W. Ammerman, R.R. Hood, D.A. Case, J.B. Cotner
Phosphorus deficiency in the Atlantic: an emerging paradigm in oceanography
EOS Trans. Am. Geophys. Union, 84 (2003), pp. 165–170

E.T. Arning, A. Lueckge, C. Breuer, N. Gussone, D. Birgel, J. Peckmann
Genesis of phosphorite crusts off Peru
Mar. Geol., 262 (2009), pp. 68–81

W. Bach, S. Roberts, D.A. Vanko, R.A. Binns, C.J. Yeats, P.R. Craddock, S.E. Humphris
Controls of fluid chemistry and complexation on rare-earth element contents of anhydrite from the Pacmanus subseafloor hydrothermal system, Manus Basin, Papua New Guinea
Miner. Deposita, 38 (2003), pp. 916–935

M. Bau, P. Dulski
Evolution of the yttrium–holmium systematics of seawater through time
Mineral. Mag., 58A (1994), pp. 61–62

M. Bau, P. Dulski
Distribution of yttrium and rare-earth elements in the Penge and Kuruman iron-formations, Transvaal Supergroup, South Africa
Precambr. Res., 79 (1996), pp. 37–55

M. Bau, P. Dulski
Comparing yttrium and rare earths in hydrothermal fluids from the Mid-Atlantic Ridge: implications for Y and REE behaviour during near-vent mixing and for the Y/Ho ratio of Proterozoic seawater
Chem. Geol., 155 (1999), pp. 77–90

M. Bau, A. Koschinsky, P. Dulski, J.R. Hein
Comparison of the partitioning behaviours of yttrium, rare earth elements, and titanium between hydrogenetic marine ferromanganese crusts and seawater
Geochim. Cosmochim. Acta, 60 (1996), pp. 1709–1725

M. Bau, P. Möller, P. Dulski
Yttrium and lanthanides in eastern Mediterranean seawater and their fractionation during redox-cycling
Mar. Chem., 56 (1997), pp. 123–131

M. Bau, S. Balan, K. Schmidt, A. Koschinsky
Rare earth elements in mussel shells of the Mytilidae family as tracers for hidden and fossil high-temperature hydrothermal systems
Earth Planet. Sci. Lett., 299 (2010), pp. 310–316

N.B. Bekasova
Pechenga (Kola Peninsula) paleogeography in early Pilgujärvi time of the early Proterozoic
Lithol. Min. Resour., 20 (1985), pp. 127–137

N.B. Bekasova, O.B. Dudkin
Composition and nature of early Precambrian Pechenga concretionary phosphorites (Kola peninsula)
Lithol. Min. Resour., 6 (1981), pp. 107–113 (in Russian)

A. Bekker, K.A. Eriksson
Paleoproterozoic drowned carbonate platform on the southeastern margin of the Wyoming Craton: a record of the Kenorland breakup
Precambr. Res., 120 (2003), pp. 327–364

A. Bekker, H.D. Holland
Oxygen overshoot and recovery during the early Paleoproterozoic
Earth Planet. Sci. Lett., 317 (2012), pp. 295–304

A. Bekker, H.D. Holland, P.L. Wang, D. Rumble, H.J. Stein, J.L. Hannah, L.L. Coetzee, N.J. Beukes
Dating the rise of atmospheric oxygen
Nature, 427 (2004), pp. 117–120

A. Bekker, J.F. Slack, N. Planavsky, B. Krapez, A. Hofmann, K.O. Konhauser, O.J. Rouxel
Iron formation: the sedimentary product of a complex interplay among mantle, tectonic, oceanic, and biospheric processes
Econ. Geol., 105 (2010), pp. 467–508

R.H. Byrne, E.R. Sholkovitz
Marine chemistry and geochemistry of lanthanides
K.A. Gschneidner, L. Eyring (Eds.), Handbook on the Physics and Chemistry of Rare Earths, Elsevier Science B.V. (1996), pp. 497–593

D.E. Canfield
The early history of atmospheric oxygen: Homage to Robert M. Garrels
Annu. Rev. Earth Planet. Sci., 33 (2005), pp. 1–36

A.E. Črne, V.A. Melezhik, A.R. Prave, A. Lepland, A.E. Romashkin, D.V. Rychanchik, E.J. Hanski, Z. Luo
Zaonega formation: FAR-DEEP holes 12A and 12B, and neighbouring quarries
V.A. Melezhik, A.R. Prave, A.E. Fallick, E.J. Hanski, A. Lepland, L.R. Kump, H. Strauss (Eds.), Reading the Archive of Earth's Oxygenation: Volume 2: The Core Archive of the Fennoscandian Arctic Russia - Drilling Early Earth Project, Springer (2013), pp. 946–1007

G.M. Filippelli
The global phosphorus cycle
M.J. Kohn, J. Rakovan, J.M. Hughes (Eds.), Phosphates: Geochemical, Geobiological, and Materials Importance (2005), pp. 391–425

G.M. Filippelli
The global phosphorus cycle: past, present, and future

Elements, 4 (2008), pp. 89–95

K.B. Föllmi
The phosphorus cycle, phosphogenesis and marine phosphate-rich deposits
Earth Sci. Rev., 40 (1996), pp. 55–124

P.N. Fröelich, M.L. Bender, N.A. Luedtke, G.R. Heath, T. Devries
The marine phosphorus cycle
Am. J. Sci., 282 (1982), pp. 474–511

C.R. Glenn, M.A. Arthur
Petrology and major element geochemistry of peru margin phosphorites and associated diagenetic minerals – authigenesis in modern organic-rich sediments
Mar. Geol., 80 (1988), pp. 231–267

C. Gärtner, H. Bahlburg, A.P. Martin, D.J. Condon, A.R. Prave, A. Lepland, J. Berndt, A. Gerdes
Detrital zircon geochronology and provenance analysis for Paleoproterozoic siliciclastic sediments of the Fennoscandian Shield (extended abstract)
IODP/ICDP Kolloquium, Münster, 14–16 March 2011 (2011), pp. 63–66

B.A. Haley, G.P. Klinkhammer, J. McManus
Rare earth elements in pore waters of marine sediments
Geochim. Cosmochim. Acta, 68 (2004), pp. 1265–1279

J.L. Hannah, H.J. Stein, A. Zimmerman, G. Yang, R.J. Markey, V.A. Melezhik
Precise 2004 ± 9 Ma Re–Os age for Pechenga black shale: Comparison of sulfides and organic material
Geochim. Cosmochim. Acta, 70 (2006), p. A228

E.J. Hanski, H. Huhma, V.F. Smol'kin, M. Vaasjoki
The age of ferropicritic volcanites and comagmatic Ni-bearing intrusions at Pechenga, Kola Peninsula, U.S.S.R
Geol. Surv. Finland Bull., 62 (1990), pp. 123–133

E.J. Hanski, H. Huhma, V.A. Melezhik
New isotopic and geochemical data from the Palaeoproterozoic Pechenga Greenstone Belt, NW Russia: implication for basin development and duration of the volcanism
Precambr. Res., 245 (2014), pp. 51–65

D. Herwartz, T. Tutken, K.P. Jochum, P.M. Sander
Rare earth element systematics of fossil bone revealed by LA-ICPMS analysis
Geochim. Cosmochim. Acta, 103 (2013), pp. 161–183

H.D. Holland
Volcanic gases, black smokers, and the great oxidation event
Geochim. Cosmochim. Acta, 66 (2002), pp. 3811–3826

R.A. Jahnke
The synthesis and solubility of carbonate fluorapatite
Am. J. Sci., 284 (1984), pp. 58–78

I. Jarvis, W.C. Burnett, Y. Nathan, F.S.M. Almbaydin, A.K.M. Attia, L.N. Castro, R. Flicoteaux, M.E. Hilmy, V. Husain, A.A. Qutawnah, A. Serjani, Y.N. Zanin
Phosphorite geochemistry – state-of-the-art and environmental concerns
Eclogae Geol. Helv., 87 (1994), pp. 643–700

K.P. Jochum, U. Weis, B. Stoll, D. Kuzmin, Q.C. Yang, I. Raczek, D.E. Jacob, A. Stracke, K. Birbaum, D.A. Frick, D. Gunther, J. Enzweiler

Determination of reference values for NIST SRM 610-617 glasses following ISO guidelines
Geostand. Geoanal. Res., 35 (2011), pp. 397–429

L. Joosu, A. Lepland, K. Kirsimäe, A.E. Romashkin, N.M.W. Roberts, A.P. Martin, A.E. Črne
The REE-composition and petrography of apatite in 2.0 Ga zaonega Formation, Russia: the environmental setting for phosphogenesis
Chem. Geol., 395 (2015), pp. 88–107

A.J.R. Kent, C.A. Ungerer
Production of barium and light rare earth element oxides during LA-ICP-MS microanalysis
J. Anal. At. Spectrom., 20 (2005), pp. 1256–1262

A.C. Knudsen, M.E. Gunter
Sedimentary phosphorites – an example: phosphoria formation, Southeastern Idaho, USA
M.J. Kohn, J. Rakovan (Eds.), Phosphates: Geochemical, Geobiological, and Materials Importance, 48 (2002), pp. 363–389

K.P. Krajewski, P. Vancappellen, J. Trichet, O. Kuhn, J. Lucas, A. Martinalgarra, L. Prevot, V.C. Tewari, L. Gaspar, R.I. Knight, M. Lamboy
Biological processes and apatite formation in sedimentary environments
Eclogae Geol. Helv., 87 (1994), pp. 701–745

A. Lepland, V.A. Melezhik, A.E. Papineau, A.E. Romashkin, L. Joosu
The earliest phosphorites – radical change in the phosphorus cycle during the palaeoproterozoic
V.A. Melezhik, A.R. Prave, A.E. Fallick, L.R. Kump, H. Strauss, A. Lepland, E. Hanski (Eds.), Reading the Archive of Earth's Oxygenation: Volume 3: Global Events and the Fennoscandian Arctic Russia – Drilling Early Earth Project, Springer (2013), pp. 1275–1296

A. Lepland, L. Joosu, K. Kirsimäe, A.R. Prave, A.E. Romashkin, A.E. Crne, A.P. Martin, A.E. Fallick, P. Somelar, K. Üpraus, K. Mand, N.M.W. Roberts, M.A. van Zuilen, R. Wirth, A. Schreiber
Potential influence of sulphur bacteria on Palaeoproterozoic phosphogenesis
Nat. Geosci., 7 (2014), pp. 20–24

H.F. Ling, X. Chen, D. Li, D. Wang, G.A. Shields-Zhou, M.Y. Zhu
Cerium anomaly variations in Ediacaran-earliest Cambrian carbonates from the Yangtze Gorges area, South China: implications for oxygenation of coeval shallow seawater
Precambr. Res., 225 (2013), pp. 110–127

Y.G. Liu, M.R.U. Miah, R.A. Schmitt
Cerium – a chemical tracer for paleo-oceanic redox conditions
Geochim. Cosmochim. Acta, 52 (1988), pp. 1361–1371

T.W. Lyons, C.T. Reinhard, N.J. Planavsky
The rise of oxygen in Earth's early ocean and atmosphere
Nature, 506 (2014), pp. 307–315

A.P. Martin, A.P. Prave, D.J. Condon, A. Lepland, A.E. Fallick, A.E. Romashkin, P.V. Medvedev, D.V. Rychanchik
Multiple palaeoproterozoic carbon burial episodes and excursions
Earth Planet. Sci. Lett., 424 (2015), pp. 226–236

A. Mazumdar, D.M. Banerjee, M. Schidlowski, V. Balaram
Rare-earth elements and stable isotope geochemistry of early Cambrian chert-phosphorite assemblages from the Lower Tal formation of the Krol Belt (Lesser Himalaya, India)
Chem. Geol., 156 (1999), pp. 275–297

S.M. McLennan
Rare-earth elements in sedimentary-rocks – influence of provenance and sedimentary processes

Rev. Mineral., 21 (1989), pp. 169–200
Loading

V.A. Melezhik, E.J. Hanski
The pechenga greenstone belt
V.A. Melezhik, A.R. Prave, E.J. Hanski, A.E. Fallick, A. Lepland, L.R. Kump, H. Strauss (Eds.), Reading the Archive of Earth's Oxygenation: Volume 1: The Paleoproterozoic of Fennoscandia as Context for the Fennoscandian Arctic Russia – Drilling Early Earth Project, Springer (2013), pp. 289–385

V.A. Melezhik, B.A. Sturt
General geology and evolutionary history of the early Proterozoic polmak-pasvik-pechenga-imandra varzuga-ustponoy greenstone-belt in the northeastern Baltic shield
Earth Sci. Rev., 36 (1994), pp. 205–241

V.A. Melezhik, B.A. Sturt
The early Proterozoic Pechenga-Varzuga Belt: a case of Precambrian back-arc spreading by Evgenii V. Sharkov and Valery F. Smolkin (1997) – Precambrian Research 82, 133-151
Comment Precambr. Res., 92 (1998), pp. 215–218

V.A. Melezhik, A.E. Fallick, E.J. Hanski, L. Kump, A. Lepland, A. Prave, H. Strauss
Emergence of the modern earth system during the archean-proterozoic transition
GSA Today, 15 (2005), pp. 4–11

A. Michard, G. Michard, D. Stuben, P. Stoffers, J.L. Cheminee, N. Binard
Submarine thermal springs associated with young volcanos – the Teahitia Vents, Society Islands, Pacific-Ocean
Geochim. Cosmochim. Acta, 57 (1993), pp. 4977–4986

S. Morad, S. Felitsyn
Identification of primary Ce-anomaly signatures in fossil biogenic apatite: implication for the Cambrian oceanic anoxia and phosphogenesis
Sed. Geol., 143 (2001), pp. 259–264

M.T. Neary, D.G. Reid, M.J. Mason, T. Friscic, M.J. Duer, M. Cusack
Contrasts between organic participation in apatite biomineralization in brachiopod shell and vertebrate bone identified by nuclear magnetic resonance spectroscopy
J. R. Soc. Interface, 8 (2011), pp. 282–288

G.J. Nelson, P.K. Pufahl, E.E. Hiatt
Paleoceanographic constraints on Precambrian phosphorite accumulation, Baraga Group, Michigan, USA
Sed. Geol., 226 (2010), pp. 9–21

Y. Nozaki, J. Zhang, H. Amakawa
The fractionation between Y and Ho in the marine environment
Earth Planet. Sci. Lett., 148 (1997), pp. 329–340

D. Papineau
Global biogeochemical changes at both ends of the Proterozoic: insights from phosphorites
Astrobiology, 10 (2010), pp. 165–181

C.A. Partin, A. Bekker, N.J. Planavsky, C.T. Scott, B.C. Gill, C. Li, V. Podkovyrov, A. Maslov, K.O. Konhauser, S.V. Lalonde, G.D. Love, S.W. Poulton, T.W. Lyons
Large-scale fluctuations in Precambrian atmospheric and oceanic oxygen levels from the record of U in shales
Earth Planet. Sci. Lett., 369–370 (2013), pp. 284–293

J. Peñuelas, B. Poulter, J. Sardans, P. Ciais, M. van der Velde, L. Bopp, O. Boucher, Y. Godderis, P. Hinsinger, J. Llusia, E. Nardin, S. Vicca, M. Obersteiner, I.A. Janssens
Human-induced nitrogen–phosphorus imbalances alter natural and managed ecosystems across the globe
Nat. Commun., 4 (2013), pp. 1–10

D.Z. Piper, M. Bau
Normalized rare earth elements in water, sediments, and wine: identifying sources and environmental redox conditions
Am. J. Anal. Chem., 4 (2013), pp. 69–83

N. Planavsky, A. Bekker, O.J. Rouxel, B. Kamber, A. Hofmann, A. Knudsen, T.W. Lyons
Rare earth element and yttrium compositions of Archean and Paleoproterozoic Fe formations revisited: new perspectives on the significance and mechanisms of deposition
Geochim. Cosmochim. Acta, 74 (2010), pp. 6387–6405

G. Postma
Slumps and their deposits in fan delta front and slope
Geology, 12 (1984), pp. 27–30

I.S. Puchtel, G.E. Brugmann, A.W. Hofmann
Precise Re–Os mineral isochron and Pb–Nd–Os isotope systematics of a mafic-ultramafic sill in the 2.0 Ga Onega plateau (Baltic Shield)
Earth Planet. Sci. Lett., 170 (1999), pp. 447–461
Loading

P.K. Pufahl, E.E. Hiatt
Oxygenation of the Earth's atmosphere-ocean system: a review of physical and chemical sedimentologic responses
Mar. Pet. Geol., 32 (2012), pp. 1–20

B. Reynard, C. Lecuyer, P. Grandjean
Crystal-chemical controls on rare-earth element concentrations in fossil biogenic apatites and implications for paleoenvironmental reconstructions
Chem. Geol., 155 (1999), pp. 233–241

A.Y. Rozanov, M.M. Astafieva
Prasinophyceae (green algae) from the lower Proterozoic of the Kola Peninsula
Paleontol. Zh., 4 (2008), pp. 90–93

A.Y. Rozanov, M.M. Astafieva, R.B. Hoover
Instruments, Methods, and Missions for Astrobiology, X, 6694 (2007), p. 6694

K.C. Ruttenberg
The global phosphorus cycle
643

J. Schijf, H.J.W. de Baar, J.R. Wijbrans, W.M. Landing
Dissolved rare earth elements in the Black Sea
Deep-Sea Res., 38 (1991), pp. 805–823

H.N. Schulz, H.D. Schulz
Large sulfur bacteria and the formation of phosphorite
Science, 307 (2005), pp. 416–418

G. Shields, P. Stille
Diagenetic constraints on the use of cerium anomalies as palaeoseawater redox proxies: an isotopic and REE study of Cambrian phosphorites

Chem. Geol., 175 (2001), pp. 29–48

J.F. Slack, T. Grenne, A. Bekker, O.J. Rouxel, P.A. Lindberg
Suboxic deep seawater in the late Paleoproterozoic: evidence from hematitic chert and iron formation related to seafloor-hydrothermal sulfide deposits, central Arizona, USA
Earth Planet. Sci. Lett., 255 (2007), pp. 243–256

J.C. Taylor
Computer programs for standardless quantitative analysis of minerals using the full powder diffraction profile
Powder Diffr., 6 (1991), pp. 2–9

Taylor S. R. and McLennan S. M. (1985) *The Continental Crust: Its composition and evolution: an examination of the geochemical record preserved in sedimentary rocks*, Blackwell, Oxford, pp. 312.

C.N. Trueman
Chemical taphonomy of biomineralized tissues
Palaeontology, 56 (2013), pp. 475–486

T. Tyrell
The relative influences of nitrogen and phosphorus on oceanic primary production
Nature, 400 (1999), pp. 525–531

P.M. Vitousek, S. Porder, B.Z. Houlton, O.A. Chadwick
Terrestrial phosphorus limitation: mechanisms, implications, and nitrogen–phosphorus interactions
Ecol. Appl., 20 (2010), pp. 5–15

R.J. Walker, J.W. Morgan, E. Hanski, V.F. Smolkin
Re–Os systematics of early Proterozoic ferropicrites, Pechenga Complex, NW Russia: evidence for ancient 187Os-enriched plumes
Geochim. Cosmochim. Acta, 61 (1997), pp. 3145–3160

J. Wright, H. Schrader, W.T. Holser
Paleoredox variations in ancient oceans recorded by rare-earth elements in fossil apatite
Geochim. Cosmochim. Acta, 51 (1987), pp. 631–644